ISSN 1811-2382, Polymer Science, Series C, 2018, Vol. 60, Suppl. 1, pp. S135–S147. © Pleiades Publishing, Ltd., 2018.

# Chirality in Self-Assembling Rod-Coil Copolymers: Macroscopic Homochirality Versus Local Chirality[1]

**Yu. A. Kriksin[a], I. I. Potemkin[b,c,d], and P. G. Khalatur[e,f,*]**

[a] *Keldysh Institute of Applied Mathematics, Russian Academy of Sciences, Moscow, 125047 Russia*
[b] *Physics Department, Lomonosov Moscow State University, Moscow, 119991 Russia*
[c] *DWI—Leibniz Institute for Interactive Materials, Aachen, 52056 Germany*
[d] *National Research South Ural State University, Chelyabinsk, 454080 Russia*
[e] *Institute of Organoelement Compounds, Russian Academy of Sciences, Moscow, 119991 Russia*
[f] *Institute of Advanced Energy-Related Nanomaterials, University of Ulm, Ulm, D-89081 Germany*
**e-mail: khalatur@polly.phys.msu.ru*

Received March 12, 2018

**Abstract**—We study chiral mesophases arising as a result of the interplay between microphase separation and orientational ordering in diblock rod-coil copolymers. It is shown that nearly compositionally symmetric copolymers form a columnar structure with twisted rod-rich domains, whereas there is a suppression of the lamellar morphologies with respect to the columnar one. Using high-resolution three-dimensional self-consistent field simulations, we show that chirality in the unit cell of the hexagonal phase develops in two different ways, leading to either homochiral state or heterochiral (locally chiral) state. Thus, chiral polarization, which occurs when the rigid and flexible blocks are segregated, causes a transition to two degenerate chiral states. In a system with many twisted domains, the magnitude of the chirality charge obeys the binomial distribution with random selection of the twist direction for each of the rod-rich domains. We suggest a model of pseudo-dynamical structural evolution aimed at understanding of how chirality arises from the achiral state and how it evolves. At the initial stage of the evolutionary process, there exists some waiting time for the onset of irreversible changes in chirality; during this time the system flips between the two chirality states.

**DOI:** 10.1134/S1811238218020133

## INTRODUCTION

Copolymers consisting of flexible and rigid segments expand the scope and complexity of microphase separation phenomena. Due to the highly disparate aspect ratios of coil and rod segments, rod-coil copolymers (RCCs) are capable of self-assembling into a large variety of nanostructures with unique architectures and properties. In this connection, it is no great surprise that in the last decade, various theoretical and numerical approaches have been extensively used for studying the rich phase behavior in RCCs [1–5]. In particular, the numerical implementation of self-consistent field theory (SCFT) [6, 7] has been applied in several publications [8–21]. It should be noted, however, that despite the considerable advances of the SCFT method, as applied to RCCs, it is notable that until now only oversimplified one- and two-dimensional (1D and 2D) model systems of RCCs have been studied. Although various morphologies have been observed in these simulations, no three-dimensional (3D) continuous SCFT calculation on the RCCs with the orientational interaction has been reported before the publication of our results [22]. The 3D SCFT studies of worm-like [23, 24] and rod-coil [25] copolymers were carried out only recently.

In order to adequately describe the equilibrium microphase separated morphologies formed via self-assembly by RCCs, numerical SCFT simulations must be implemented in the 3D space for large systems with high spatial resolution. Such studies are needed in order to distinguish between thermodynamically stable structures and metastable structures that often survive in low-dimensional systems. Moreover, certain types of equilibrium structures, which can arise in reality, may never occur in low-dimensional systems. It should also be kept in mind that due to long wavelength fluctuations, mean-field theories describe order-disorder phenomena often very inaccurate at low dimensionality.

To theoretically understand the phase behavior of flexible block copolymers, two main parameters are introduced: the isotropic Flory–Huggins interaction parameter $\chi$ and the copolymer composition $f$. For the microphase-separating RCC systems, additional parameters are required to characterize the anisotro-

[1] The article is published in the original.

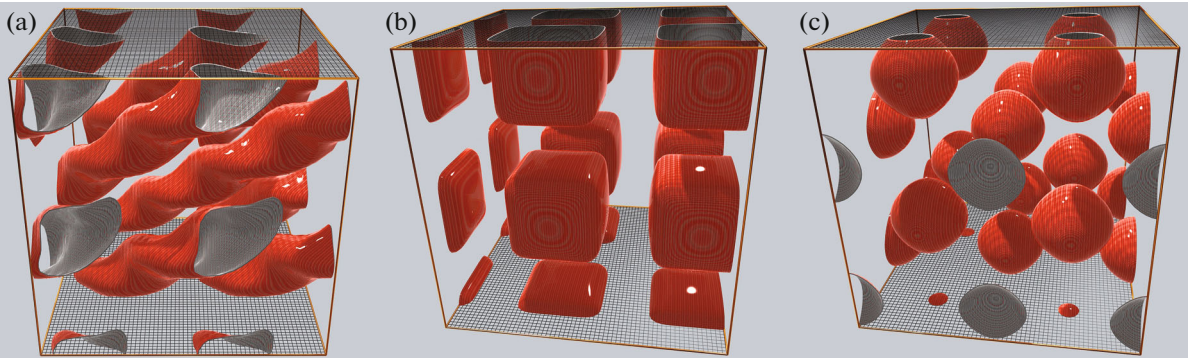


**Fig. 1.** (Color online) Examples of stable periodic structures predicted from the SCFT simulation [22]: (a) chiral hexagonal phase HEX* ($f = 0.5$ and $\chi N = 14$); (b) achiral phase with nearly cubic rod-rich domains ($f = 0.625$ and $\chi N = 16$); (c) achiral BCC-like phase ($f = 0.75$ and $\chi N = 16$). Here, $f$ is the fraction of flexible blocks and $N$ is the total number of chain segments. The surface represents the interface between the coil-rich domains and the rod-rich domains. The rigid blocks are located inside closed regions. The matrix consists of the flexible-chain segments. Adapted from [22].

pic orientational interaction of rigid rodlike blocks and their shape. Because of the coupling between orientational ordering and block incompatibility/stretching, RCCs are able to self-organize into various 3D nanostructures, depending on different combinations of these parameters.

Previously, we have presented an efficient parallel algorithm for the high-resolution 3D SCFT simulations of RCCs with a Maier-Saupe-type mean field orientational interaction accounting for the coupling of the rodlike segments [22]. The parallelization was achieved using a 2D domain decomposition strategy (also known as "pencil" or "drawer" decomposition) for fast Fourier transform (FFT) which is employed for solving the modified diffusion equations via a pseudo-spectral (PS) collocation technique. The FFT-based trigonometric interpolation and Gauss-Legendre or Lebedev quadratures were utilized for evaluating the angle-dependent integrals. To accelerate the convergence of the iterative process, the parallel Ng method was used. With this numerical implementation of SCFT, it was possible to reveal a variety of new intrinsic 3D structures and particularly identify one interesting morphology of hexagonally arranged chiral cylinders [22, 26–28], which has not been previously reported for rod-coil diblocks or related systems and cannot be predicted theoretically in low-dimensional space. Some of these structures are shown in Fig. 1.

A rather unexpected result was that hexagonal morphology is formed for compositionally symmetric RCCs, whereas flexible block copolymers with the same composition self-organize into lamellae. A specific feature of this structure is that hexagonally (HEX) packed columnar domains are twisted around their long axes like a corkscrew (HEX* phase, Fig. 1a), thereby producing chirality. Except for the HEX* phase, all others were found to be metastable at the coil fraction $f$ close to 0.5. For the diblocks with a coil fraction of ≈0.6, two morphologies were predicted: a structure with nearly cubic domains packed into a simple cubic (SC) lattice (Fig. 1b) and truncated polyhedrons arranged in a body-centered cubic (BCC) lattice. The free energy of both structures practically does not differ. Finally, only BCC-like stable structure with space group $Pm\bar{3}m$ was observed at $f > 0.7$ (Fig. 1c). In these micellar structures, the rigid segments tend to be parallel or antiparallel in the micelle interior because of the restrictions caused by conditions of packing. Therefore, there are polyhedra instead of geometrically perfect spherical microdomains in the conventional BCC morphology (Figs. 1b, 1c). Unlike the HEX* phase, the micellar phases are achiral due to the inherent reflection planes.

There is an active current search for routes to create chiral structures from achiral molecules and for mechanisms responsible for the appearance of chirality. The scale of interest is ranged from nanometers to micrometers and beyond, which reveals the most interesting features of chirality in chemistry, materials sciences and biology. The origin of the mirror symmetry breaking at the molecular level is also a long-standing question in molecular evolution. However, the relationship between the molecular and macroscopic levels remains far from being understood. In this study, we apply a continuum RCC model and use our SCFT computational technique [22] (see also [29–31]) to investigate in more detail the chiral properties of the columnar structure arising in the system from the packing of achiral building blocks. In particular, we are going to answer the following question: is this phase macroscopically chiral (that is, can molecular chirality propagates over macroscopic distances) or does it have only local chirality restricted by rod-rich domains?

The paper proceeds as follows. The SCFT model and computational scheme are briefly described and the results are discussed. First, to understand the

twisting mechanism responsible for the confinement-induced chirality in the self-assembly of RCCs, we introduce a simple theoretical formalism in terms of interfacial curvature and packing frustration for the strong segregation regime. Next, using the SCFT calculations, we explore both global and local chirality of the hexagonal mesophase. Our goal here is to understand how chirality is distributed across columnar domains in the unit cell. Then we investigate chiral degeneracy of the hexagonal ground state. Finally, some issues related to the chirality evolution are reported. Conclusions are summarized in Concluding remarks section.

## SCFT MODEL AND COMPUTATIONAL SCHEME

The RCC model and SCFT approach have been presented by Pryamitsyn and Ganesan [12] and here will be only briefly introduced. Differently from [12] (see also [13]), where 1D and 2D models were employed, we will consider a 3D system. The system is composed of $n$ monodisperse RCC chains in volume $V$. The coil (A) block is assumed to be completely flexible with a Kuhn segment length $a$, and the rod (B) block is completely rigid. The coil and rod blocks consist of $fN$ and $(1 - f)N$ segments, respectively, and therefore the total number of segments in the copolymer is $N$. We denote the position of the $i$th segment by $\mathbf{r}_i$ and the orientation of the $i$th rod by $\mathbf{u}_i$. We neglect the chirality of rod blocks; that is, all corresponding functions should be invariant with respect to flip $\mathbf{u} \to -\mathbf{u}$. All lengths are scaled by $R_g = a(N/6)^{1/2}$ and the relative length of the rod is defined by the microscopic parameter $\gamma$ [12].

Since the polymer self-consistent-field theory has been well developed, we only provide a brief summary of the SCFT calculations here; readers are referred to e.g. [22] for detailed derivation and explanation of this approach. The total system Hamiltonian is assumed to be $H = H^{(0)} + H^{(1)} + H^{(2)}$, where $H^{(0)}$ comes from stretching of each chain and specifies the ideal (entropic) contribution, $H^{(1)}$ comes from the effective segment-segment repulsion that is determined by Flory-Huggins parameter $\chi$, and $H^{(2)}$ characterizes a Maier–Saupe (MS)-type mean field orientational interaction. The strength of the anisotropic orientational interaction favoring the alignment of the rods is quantified by MS energy parameter $\mu$. The theoretical description of the phase behavior of RCCs requires the introduction of a compositional (density) order parameter, $\phi_\alpha(\mathbf{r})$, and an orientational order parameter, $\eta(\mathbf{r})$. The $\eta(\mathbf{r})$ may vary from 0 in an isotropic phase to 1 when the segments are aligned perfectly parallel.

As is customary in the SCFT [7], the interactions between a chain segment and its neighbors in the bulk are replaced with the interactions of the segment with external fields $w_\alpha(\mathbf{r})$ and $\mathbf{M}(\mathbf{r})$ that represent the isotropic and anisotropic interactions, respectively, with all neighbors in a many-chain system and are equivalent to the chemical potential fields conjugated to the local density fields $\phi_\alpha(\mathbf{r})$ and the local orientational order parameters $\eta(\mathbf{r})$, which in turn depend self-consistently on the corresponding potential fields. Note that $\mathbf{M}(\mathbf{r})$ is a tensorial field. In the mean-field approximation, one makes the assumption that there is a single set of "saddle point" field configurations that dominates the partition function [7]. When the saddle point mean fields $w^*(\mathbf{r})$ and $\mathbf{M}^*(\mathbf{r})$ are known, in principle, any property of the many-chain system, including its free energy $F$, can be accessed. In this approximation, the SCFT equations are obtained by minimizing the system Hamiltonian with respect to the potential fields at the saddle point of $H$. These equations are solved numerically by an iterative technique, which yields density fields and orientational order parameters at point $\mathbf{r}$. For a 3D system of RCCs, such calculations can easily become extremely computationally demanding as the size (resolution) of the simulated system increases, exceeding what conventional small clusters can provide, thus making massively parallel computing a necessity. As mentioned in the Introduction, we developed an efficient parallel algorithm for the large-scale, high-resolution 3D SCFT simulations [22]. Based on this technique, a modified diffusion equation was solved using the pseudo-spectral operator splitting approach [6, 7] and 2D domain decomposition for Fast Fourier Transform (FFT). The FFT-based trigonometric interpolation and the Lebedev-Laikov (LL) quadrature [32] were utilized in this study for evaluating the angle-dependent integrals. In order to reduce the influence of the computational cell shape/size on final morphologies, the system free energy was minimized with respect to the cell parameters [22, 29], using the hexagonal basis $\mathbf{t}_i^2 = D^2$, $\mathbf{t}_1 \cdot \mathbf{t}_2 = D^2/2$ and $\mathbf{t}_1 \cdot \mathbf{t}_3 = \mathbf{t}_2 \cdot \mathbf{t}_3 = 0$, where $D_i = |\mathbf{t}_i|$ is the cell edge length ($i = 1, 2, 3$) and the basis of the cell $\{\mathbf{t}_1, \mathbf{t}_2, \mathbf{t}_3\}$ defines the set of the translation vectors.

The phase behavior of rod-coil diblocks is determined by their chemical composition $f$, the Flory-Huggins parameter $\chi$ and the MS parameter $\mu$. Since the dimension of the parameter space in our model is large to explore all possible combinations, below we will restrict ourselves to the case of relatively weak orientational interaction ($\mu/\chi = 1.3$) and the symmetric diblock copolymers with $f = 0.5$. We note that the $\mu/\chi$ ratio of the order of 1 is quite typical for many RCCs with the microphase separated morphologies. Representative examples are the poly-(diethylhexyloxy-*p*-phenylenevinylene)-*b*-(styrene) (DEH-PPV-*b*-PS) block copolymers containing $\pi$-conjugated rod-like segments [33]. It should be stressed that when the $\mu/\chi$ ratio is close to unity, the orientational interaction is not so large that the microphase-separating system tends to form into a large area of lamellar structures by

rods aligning with each other. Following Pryamitsyn and Ganesan [12] the parameter $\gamma$ was fixed to be $\gamma = 16.33$.

In our previous work [22, 26–28], it was shown that the compositionally symmetric RCCs form the conventional hexagonal mesophase (HEX), which is stable in the range $8.8 \le \chi N < 13.1$. Importantly, the order-disorder transition (ODT) occurs at much lower $\chi N$ than that known for coil-coil diblock copolymers. Indeed, on the basis of a Landau theory, Leibler predicted a critical point of microphase separation at $\chi N = 10.495$ and $f = 0.5$ for a compositionally and conformationally symmetric flexible-chain diblocks [34]. Moreover, a microphase separation critical point does not exist in a RCC system because RCC diblocks lack the conformational symmetry (the free energy is not invariant when the two rigid and flexible blocks interchange their volume fractions). The chiral morphology HEX* with twisted hexagonally packed columnar domains (Fig. 1a) arises at $\chi N \ge 13.1$ as a result of the phase transition HEX $\rightarrow$ HEX* from the achiral morphology. In what follows, we will discuss this chiral structure. It should be noted that the HEX* structure consists of elliptical cross-sectional columnar domains rather than from geometrically regular cylinders [22]. Therefore, although the domains are packed approximately in a hexagonal array, the six-fold rotation ($C_6$) symmetry about the cylinder axis is now destroyed. Only a two-fold rotation symmetry (the $C_2$ point-group symmetry) and a mirror symmetry still remain.

## RESULTS AND DISCUSSION

### *Chirality in the Strong Segregation Regime*

The reasons for the stability of HEX* phase and the appearance of chirality are easy to understand for the strong segregation regime, which is difficult to realize in SCFT calculations. The smectic behavior of layered RCCs was first studied in the strong segregation limit by Semenov and Vasilenko for large rod volume fractions [35]. From a microscopic viewpoint, the confinement-induced chirality is due to the competition between the interfacial energy and the elastic stretching energy of the flexible coil blocks with a certain anisotropy of the elastic properties.

In the strong segregation limit, the free energies of all microphases scale the same way with chain length $N$ and interfacial tension, so the sharp phase boundaries become independent of the strength of the repulsion $\chi$ between chemically dissimilar blocks and depend only on the copolymer composition [36]. Since amorphous and orientationally ordered liquid-crystalline (LC) regions are completely segregated, interactions between them proceed at interfaces only. Owing to the strong stretching of the flexible blocks in the amorphous phase, a hierarchy of contributions to the system free energy is a two-stage. The dominant terms are the elastic free energy of the flexible blocks and the energy of the interfaces (for example, they are $\sim(fN)^{1/3} \gg 1$ per chain in the case of the smectic C domains), whereas the ideal gas and steric contributions are on the order of unity (apart from $\pi$-conjugated rod-like segments). The ideal gas term describes the entropic losses due to the ordering, and the steric term is responsible for the free energy gain because of alignment of the rods (the latter is usually described either within the Flory or Maier-Saupe approximation [37, 38]). That is why the LC structure in the strong segregation regime is enforced by the flexible blocks and condition for the dense packing of the rods in the domains which provides minimum unfavorable contacts between the rod and coil blocks. At the first glance, nearly symmetric RCCs should form lamellar structure with the smectic A or C domains where the rods are organized in mono- or bilayers [37]. However, even in this case the hexagonal structure is stable: the HEX* columns longitudinally shrink increasing the area of the cross-section (it takes an ellipsoid rhombus shape [22]) and twisting reduces to the formation of smectic C structure in each cross-layer, however, the neighbor layers have different directors as schematically shown in Fig. 2. Such layer-to-layer alternation of the director in the strong segregation regime (the pitch of the "helix" on the order of the diameter $d$) is driven by the stretching of the flexible blocks which becomes lower in comparison with unidirectional orientation of the rods like in the lamellar structure (see Fig. 2).

The dominant contributions to the free energy per chain of the lamellar structure

$$\frac{F_L}{k_BT} = \frac{3}{2}\frac{fNv^2}{4d^4a^2}\sin^2\alpha + \frac{2\sigma d^2}{\sin\alpha} = \frac{3}{2}\left[3fN\frac{v^2\sigma^2}{a^2}\right]^{1/3}, \quad (1)$$

$$\sin\alpha = \left[\frac{8\sigma d^6a^2}{3fNv^2}\right]^{1/3}, \quad (2)$$

are the elastic free energy of the flexible blocks, $3H^2/2a^2fN$, and the interfacial energy. The space-filling condition for the amorphous layer determines its thickness, $H = fNv\ \sin\alpha/2d^2$, and factor 2 in front of the surface tension coefficient $\sigma$ corresponds to the single smectic layer. Minimization of the free energy with respect to the tilt angle $\alpha$ results in the equilibrium value (right hand side of Eq. (1)).

The free energy of the HEX* structure can easily be estimated if we assume that the flexible blocks have one-dimensional stretching like in the lamellar phase (see Fig. 2)

$$\frac{F_H}{k_BT} = \frac{3}{2}\cdot\frac{fNv^2}{16d^4a^2}\sin^2\alpha + \frac{2(\sigma+\sigma_0)d^2}{\sin\alpha} = \frac{3}{2}\left[3fN\frac{v^2\sigma^2}{a^2}\left(\frac{1+t}{2}\right)^2\right]^{1/3}, \quad (3)$$

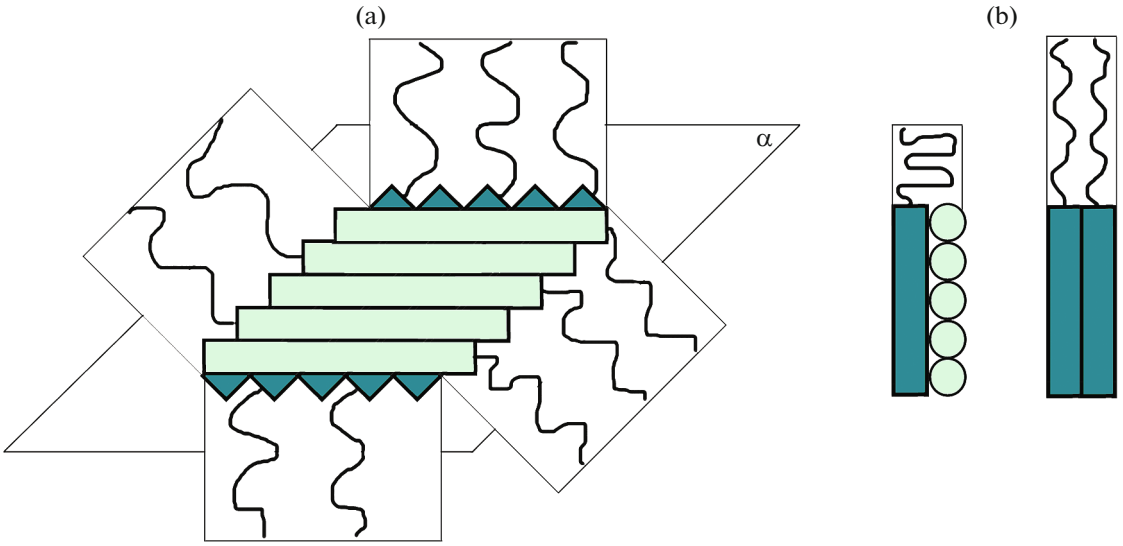


**Fig. 2.** (Color online) (a) Schematic picture of the adjacent layers of the HEX* structure in the strong segregation regime. Rectangular areas correspond to one-dimensional stretching of the flexible blocks. In reality, the area occupied by the coils, is close to the rhombus-like layer and they are less stretched than in one-dimensional approximation. (b) Different orientations of the director in the adjacent layers reduce stretching of the coils.

where $t = \sigma_0/\sigma < 1$ and $\sigma_0$ is the surface tension coefficient of the interfacial regions along the rods ($\sigma_0 < \sigma$ [39]). Such approach overestimates the elastic free energy, which in reality is lower. Figure 2 demonstrates the difference: one-dimensional stretching neglects space-filling near the corners, thus resulting in less space for the chains to explore, whereas the filling of these regions makes the thickness of the flexible-chain corona smaller. Also, the two-dimensional stretching of the chains in the corner regions is lower than one-dimensional stretching. However, even such crude 1D approximation demonstrates stability of the HEX* structure. The elastic free energy in Eq. (3) is smaller than that in Eq. (1) because the interfacial area per flexible chain is two times larger (see Fig. 2). On the other hand, the increase of the interfacial area leads to the increase of the energy (the second term in Eq. (3)). Inequality $\sigma_0 < \sigma$ (see Ref. [39]) is kept by the fact that the interface along the rod is "flat", whereas the ends of the rods make it "rough", zigzag-like in the shape. Comparing Eqs. (1) and (3), one can find that $F_H < F_L$, and the real free energy of the hexagonal structure $\tilde{F}_H$, having lower stretching of the blocks, satisfies inequality $\tilde{F}_H < F_H$. Thus, we conclude that in the strong segregation regime, nearly compositionally symmetric rod-coil block copolymers should form a hexagonal structure with twisted columnar domains.

### *Global and Local Chirality*

In this subsection, using the SCFT based results, we will analyze both global and local chirality of the hexagonally packed cylinder phase. Our goal is to understand how chirality is distributed across columnar domains in the unit cell. Unlike the qualitative theoretical formalism outlined in the previous subsection, SCFT method allows us to obtain more detailed information about the structural organization of the system.

Several dozen random starts were made in our SCFT calculations of compositionally symmetric RCCs. Having the randomly generated stable or metastable structures, we can select from them the most stable hexagonal structures with the minimum free energy. It was found that these minimal free energy configurations can exhibit various chiral properties. In other words, a chiral state corresponding to a given stable structure can be degenerate. Thus, it is instructive to select and explore such stable hexagonal structures that have different chiral properties.

Let us consider the unit cell of hexagonal phase. This cell has the shape of a rectangular parallelepiped with dimensions X, $Y = \sqrt{3}X$ and Z (Fig. 3a). The cell contains two cylindrical domains: one cylinder is located in the center of the cell and a quarter of the cylinder is located in each of the corners of the cell. Due to the periodic conditions imposed on the system, there are only two possible chiral states: homochiral state HEX* (Fig. 3a) and heterochiral state, which we will denote as HEX** (Fig. 3b). All the rod-rich domains of the HEX* phase are twisted in the same direction (clockwise or counterclockwise). In contrast, the half of the cylinders of the HEX** phase is twisted clockwise (chirality charge $q_{ch}$ is $-1$) and the other half is twisted counterclockwise ($q_{ch} = +1$). Consequently, the first structure can be characterized

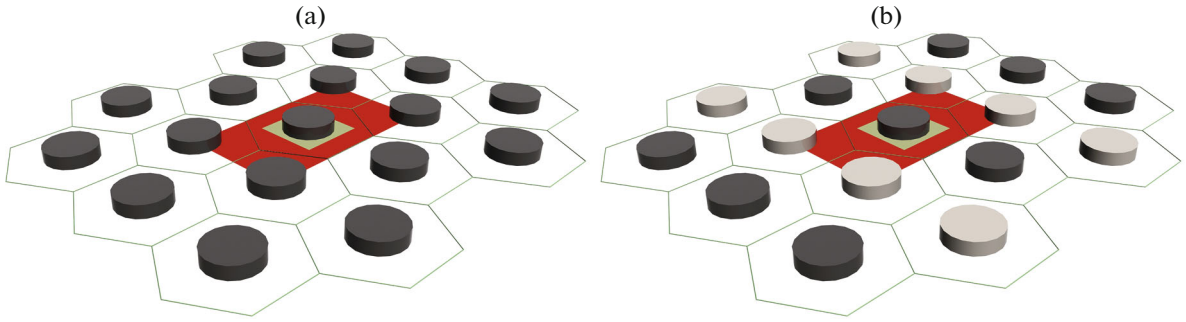


**Fig. 3.** (Color online) (a) Homochiral structure HEX* and (b) heterochiral structure HEX**. Dark cylinders show the clockwise twisting, while light cylinders depict counterclockwise twisting. The unit cell is shown as the rectangular region containing two rod-rich domains (one cylinder and four quarters of a single cylinder). The truncated subcell depicted by the square is used for calculation of the local chirality index of a single rod-rich domain.

as macroscopically homochiral, while the second structure has only local chirality. This means that the chirality of the HEX** phase can only be identified on a local length scale (see the square outlined around the central cylinder in Fig. 3), whereas the structure as a whole does not possess chirality because the total number of positive and negative chirality charges (right- or left-handed twisting directions) is the same by definition.

Chirality ("handedness") is a geometrical-topological property of many physical systems. Apart from the practical issue of the experimental identification of chirality, the natural question arises: How chiral is a given object, which is sufficiently complicated to be of interest? Speaking about the quantitative measure of chirality, it is important to note that there is a strong belief that chirality is essentially a Boolean data type and its universal measures are problematic: an object is either chiral or not. However, it is not the case. Indeed, the above-mentioned difficulty can be circumvented because molecular chirality gives rise e.g. to several chiroptical effects, which, being quantifiable, serve to classify substances as more or less chiral, thereby demonstrating different degree of chirality.

The most common quantitative measures of chirality are based on continuous pseudoscalar functions that change sign under space inversion. The well known Osipov–Pickup–Dunmur (OPD) molecular chirality index [40] is one of the first pseudoscalar geometrical measures of chirality which can be calculated numerically using the molecular structure and composition. It was scaled in order to enable a comparison of chirality for molecules of different size [41, 42] and then successfully used to predict chirality of various molecules, including proteins [43]. The OPD functional can be easily calculated for arbitrary molecular systems (discrete sets of atoms), but not for continuous periodic objects characterized by a density distribution $\rho(\mathbf{r})$. This chirality measure also ignores the fact that chirality can manifest itself in a different manner on different length scales.

To quantify the degree of chirality, we suggested a new pseudoscalar functional that may be efficiently computed for any periodic object specified by the local density as a function of continuous coordinates [26]. High computational efficiency is achieved by using a fast Fourier transform. Like the previously proposed OPD index [40], this chirality index is a pseudoscalar function, which vanishes if and only if the object is achiral, and takes equal and opposite values for an object and its mirror image. However, unlike the OPD pseudoscalar, our chirality index explicitly depends on the parameter of the linear scale on which the chirality is evaluated.

In order to quantify the global and local chirality, we introduce the corresponding continuous global and local chirality measures. The fundamental structural element of a periodic system is a unit cell that represents the most basic and least volume consuming repeating structure. The density distribution $\rho(\mathbf{r})$ in this cell determines all the structural properties, including chirality of the structure. Therefore, the unit-cell chirality index can be considered as the global chirality index (GCI). In the context of the present discussion, it is necessary to select an individual object (cylindrical domain) in the unit cell and estimate its chirality. To that end, we define a square subcell in the XY plane within the rectangular unit cell (cf. Fig. 3). This subcell includes an object of interest. In order to ensure FFT-based calculations, we impose artificial periodic boundary conditions on the subcell. The chirality index calculated from the subcell density distribution can be considered as a local chirality index (LCI). Importantly, both GCI and LCI should be distance-dependent quantities. With this in mind, as in our previous work [26], we introduce the following distance-dependent chirality index of an arbitrary 3D object characterized by some density distribution $\rho(\mathbf{r})$

$$G(\lambda; f, \rho) = I_1(\lambda; f, \rho)/I_0(\lambda; f, \rho), \quad (4)$$

where

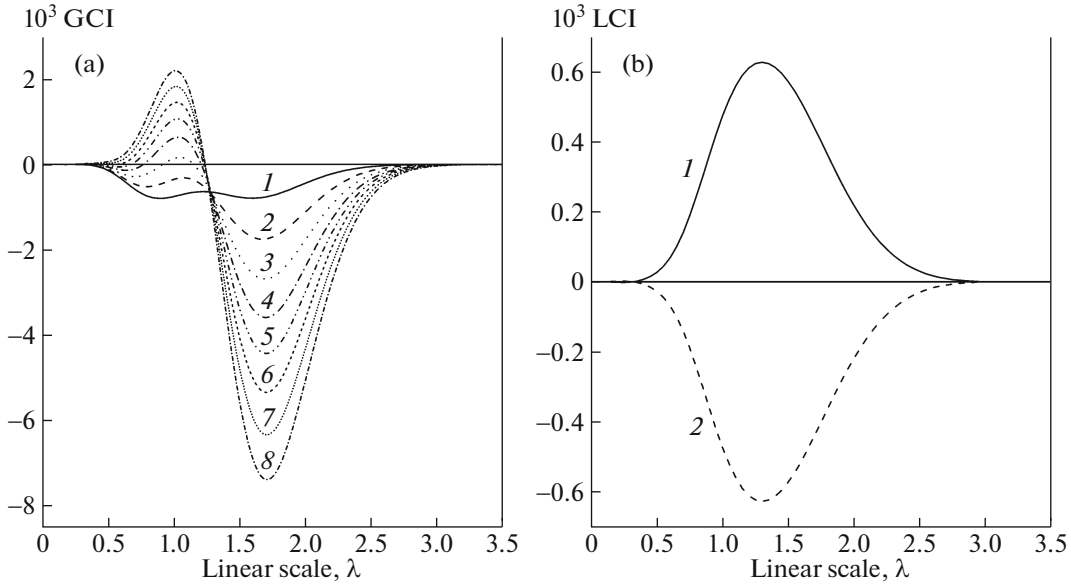


**Fig. 4.** (a) Global chirality index as a function of λ, at $f = 0.5$ and $\mu/\chi = 1.3$. $\chi N$ = (*1*) 13.1, (*2*) 13.3, (*3*) 13.5, (*4*) 13.7, (*5*) 13.9, (*6*) 14.1, (*7*) 14.3, (*8*) 14.5. (b) Local chirality index of two neighboring columnar domains (1 and 2) having chirality charges of the opposite sign as a function of λ for HEX** morphology, at $f = 0.5$, $\chi N = 13.5$ and $\mu/\chi = 1.3$.

$$I_1(\lambda; f, \rho) = \lambda^{-7}\int d^3\mathbf{r}_1 d^3\mathbf{r}_2 d^3\mathbf{r}_3 d^3\mathbf{r}_4 \rho(\mathbf{r}_1)\rho(\mathbf{r}_2)\rho(\mathbf{r}_3)\rho(\mathbf{r}_4) \times f(\lambda^{-1}r_{12}) f(\lambda^{-1}r_{23}) f(\lambda^{-1}r_{34})([\mathbf{r}_{12}\,\mathbf{r}_{34}]\mathbf{r}_{14})(\mathbf{r}_{12}\,\mathbf{r}_{23})(\mathbf{r}_{23}\,\mathbf{r}_{34}), \quad (5)$$

$$I_0(\lambda; f, \rho) = \int d^3\mathbf{r}_1 d^3\mathbf{r}_2 d^3\mathbf{r}_3 d^3\mathbf{r}_4 \rho(\mathbf{r}_1)\rho(\mathbf{r}_2)\rho(\mathbf{r}_3)\rho(\mathbf{r}_4) \times f(\lambda^{-1}r_{12}) f(\lambda^{-1}r_{23}) f(\lambda^{-1}r_{34}) \quad (6)$$

Here, $\mathbf{r}_i$ is the position vector, λ is the characteristic length scale and $f(r)$ is the Gaussian function

$$f(r) = \frac{1}{\sqrt{2\pi}^3}\exp\left(-\frac{r^2}{2\pi}\right), \quad (7)$$

which defines the spherically symmetric density distribution. The normalized density $\lambda^{-3} f(\lambda^{-1} r)$ highlights a fuzzy window of the linear scale λ to quantify chirality relating to this window (for more detail, see [26]). Note that the calculation of the $G$ functional (4) for a discrete 3D object defined by $n$ points is equivalent to a full enumeration of all possible ($\sim n^4$) irregular tetrahedra, at the vertices of which the local density is determined. The evaluation of the OPD pseudoscalar geometrical chirality index [40] is always organized in this way. For a continuous periodic system defined by its density distribution $\rho(\mathbf{r})$, the $G$ value in Eq. 4 is normalized weighted sum of chirality indices for an infinite number of tetrahedra, so that the chirality index of the system is conditional and characterizes the preponderance of tetrahedra with one orientational type over those with other types. Therefore, not the values of the chirality index themselves but rather their differences from zero for a given λ are important.

The $G$ index defined by Eqs. (4)–(7) has the following specific properties: (i) it is a quantitative measure of chirality—the larger the absolute value of the index, the more chiral the object; (ii) it vanishes for any achiral object; (iii) it changes sign when the system density $\rho(\mathbf{r})$ is replaced by its mirror image $\tilde{\rho}(\mathbf{r})$, $G(\lambda; f, \tilde{\rho}) = -G(\lambda; f, \rho)$; (iv) similarity conversion $\tilde{\rho}(\mathbf{r}) = \rho(C\mathbf{r})$ leads to $G(\lambda; f, \tilde{\rho}) = G(C\lambda; f, \rho)$. It should be borne in mind that because the chirality index $G$ is a "tetrahedron-based" functional by definition, $G = 0$ for any one- and two-dimensional objects. Also, we would like to note that the disadvantage of all pseudoscalar chirality measures is related to the so-called problem of chiral zeros: any chiral set of points can be continuously transformed into its mirror image without passing a nonchiral state [44, 45]. In other words, any pseudoscalar chirality index can turn zero despite the fact that the object is chiral. Pseudoscalar chirality measures, however, are closely related to chiral physical properties, such as molecular optical activity, the spontaneous polarization in the smectic C* liquid crystal phase [46], etc. Pseudoscalar functionals may also be used to characterize the effects of relatively small changes of the structure (including those occurring in microphase segregated copolymers) on macroscopic chiral properties.

We begin with the analysis of the global chirality index GCI calculated for homochiral phase HEX* as a function of λ at different values of $\chi N$. Some representative results are shown in Fig. 4a.

The trends displayed in this figure are not heuristically obvious. As seen, the GCI value practically vanishes when $\lambda < 0.5$ and $\lambda > 3.0$. This means that the

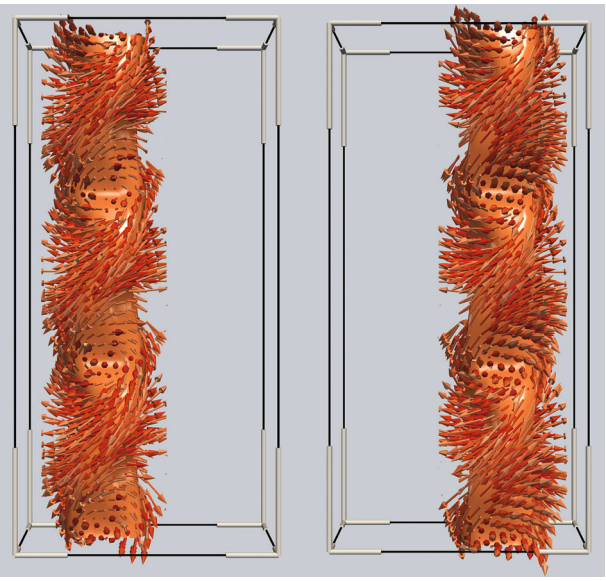

**Fig. 5.** (Color online) Orientation vector field (represented by arrows) for one of the domains in the hexagonal phase at $\chi N = 14$ and $\mu/\chi = 1.3$. The field is represented by arrows; the solid surface defines the boundaries of the domain. The maximum value of the scalar orientational order parameter is ≈0.68. Two projections are shown.

chirality manifests itself on the length scale of the order of unity (we recall that all lengths are measured in units of the radius of gyration $R_g$). An increase in $\chi N$ sharpens the $G$ profile and is accompanied by an increase in the absolute value of this index.

It is appropriate to consider the GCI value as the level of helicity relating to the chirality length scale $\lambda$. As seen in Fig. 4a, an increase in $\chi N$ has a very weak effect on the position of the global extremum. This indicates that the characteristic chirality length scale, having once emerged, remains nearly unchanged. On the other hand, an increase in the absolute value of GCI with increasing the parameter $\chi N$ can be interpreted as an increase in the *contrast* of the chiral structure. Figuratively speaking, if we identify a twisted cylindrical domain with a screw, then its thread becomes deeper with increasing the incompatibility of flexible and rigid blocks; that is, the helical motif becomes more contrast. This behavior is due to an increase in the sharpness of boundaries between regions occupied by the microphase segregated blocks.

We now turn to the analysis of the globally achiral morphology HEX** with the alternating twisted cylinders (Fig. 4b). In this case, we again consider the rectangular unit cell, but now it contains two cylinders with opposite twisting directions. It was found that in contrast to the homochiral hexagonal phase, the GCI value calculated for the HEX** phase is very close to zero for any $\chi N$ considered in the present study. At $\chi N > 13.1$, the zero value of GCI is provided by the mutual cancellation of contributions from the oppositely twisted cylinders. Nevertheless, the HEX** phase is locally chiral in the sense that the twisting of each cylinder may be revealed via the calculation of the local chirality index in a square subcell surrounding the specified cylinder. The subcell dimensions were chosen as $X_{sc} = Y_{sc} = X/2$ and $Z_{sc} = Z$. Such a choice ensures that two conditions are met: (i) the individual rod-rich columnar domain is completely placed in the subcell and (ii) the domains with the opposite twisting in the adjacent subcells are isolated from each other.

Figure 4b presents the value of LCI calculated at $\chi N = 13.5$ for two domains having chirality charges of the opposite sign. There is a marked difference between the values of GCI and LCI (compare Figs. 4a, 4b). This difference is due to the use of artificial periodic conditions. Although these periodic conditions make some perturbation, they still allow us to determine the correct chirality distribution within the domain core. From the data shown in Fig. 4b, we conclude that the two curves relating to the columnar domains of the opposite intradomain twist are in fact mirror images of each other with respect to the horizontal axis. The degree of chirality is maximum within the rod-rich domain and quickly falls off at its periphery.

Of particular interest is the local organization of the rigid blocks inside the rod-rich domains. The saddle-point orientation tensor was diagonalized to give its three eigenvalues $\xi_1(\mathbf{r})$, $\xi_2(\mathbf{r})$, and $\xi_3(\mathbf{r})$ and three corresponding eigenvectors representing the principal directions of orientation. The largest eigenvalue $\xi_{max}(\mathbf{r})$ was normalized by the volume fraction of the rod segments and multiplied by 3/2. The obtained scalar order parameter provided a measure of how well the rods are locally ordered. Having the eigenvectors corresponding to $\xi_{max}(\mathbf{r})$, one can directly visualize both the value of $\xi_{max}(\mathbf{r})$ and its direction at each grid point $\mathbf{r}$ to create an 3D representation. As an example, Fig. 5 presents the vector orientation field for one of the domains.

It is seen that within the columnar domain, the vector orientation field is distributed with a well-pronounced regular twist about the cylinder axis, forming a helical structure motif. The pitch of the helicoidal twist is determined by the balance of isotropic and anisotropic interactions. Importantly, the surface orientation of vectors is typically tangential. With perpendicular orientation relative to the interface, there would be cavities between adjacent rods, which is impossible due to incompressibility of the system. Therefore, the rods are forced to tilt in the tangential direction to avoid steric conflicts.

Thus, the performed SCFT calculations demonstrate that chirality in the unit cell of hexagonally packed cylinder phase can develop in two different ways, leading to the formation of either homochiral state with $q_{ch} = \pm 2$ or heterochiral (locally chiral) state

**Table 1.** Theoretical probability distribution of the chirality charge $q_{ch}$, the corresponding empirical frequency and its standard deviation

| Chirality charge, $q_{ch} = n - m$ | $p = P(q_{ch} = n - m)$, theoretic probability | ν, empirical frequency | σ, standard deviation of empirical frequency |
|---|---|---|---|
| −8 | 0.00391 | 0.03 | 0.00241 |
| −6 | 0.03125 | 0.02 | 0.01740 |
| −4 | 0.10938 | 0.09 | 0.03121 |
| −2 | 0.21875 | 0.20 | 0.04134 |
| 0 | 0.27344 | 0.26 | 0.04457 |
| 2 | 0.21875 | 0.18 | 0.04134 |
| 4 | 0.10938 | 0.15 | 0.03121 |
| 6 | 0.03125 | 0.04 | 0.01740 |
| 8 | 0.00391 | 0.03 | 0.00241 |

with $q_{ch} = 0$. However, the question remains: how are the twisted domains with different chiral charges distributed in a macroscopic system? Obviously, both regular and random distributions are possible. Since any iterative scheme does not provide an absolutely accurate result, the observed properties, including the chirality distribution, are of a statistical nature. Therefore, large cell SCFT calculations are needed.

### *Chiral Degeneracy of the Ground State*

In order to answer the above question, we need to perform SCFT calculations for the cell containing a sufficiently large number of rod-rich domains. To this end, we increased the dimensions of the computational cell by four times. A series of runs consisting of many independent starts with a specifically prepared initial state was carried out. Initial fields reproduced the conventional achiral hexagonal phase HEX with 8 hexagonally packed cylinders. A random (white) noise of 3% level was added to the fields, and a chaotic initial orientation of rodlike blocks was assumed. The value of $\chi N$ was set to 13.5.

Preliminary calculations showed that the choice of the iterative scheme plays an essential role. Our scheme included a series of "slow" Picard iterations and subsequent rapidly converging Ng-type iterations. The Picard iterations were intended to find new possible morphologies, while the Ng iterations were necessary for "fine tuning" of the predicted structure. We performed a sufficiently large number of Picard iterations to allow iterative sequence to wander in the state space and reveal the sets of possible solutions. If the Ng iterations are switched on too early, the conventional achiral hexagonal phase HEX is obtained. We established that about 5000 Picard iterations and $\sim 10^3$ Ng iterations are enough to generate the required number 100 of structures with different distribution of the chirality sign in cylindrical domains.

There are 256 equiprobable combinations of chirality states for 8 objects. We denote by $HEX^{mn}$ the set of all realizations of chirality charge including $m$ domains twisted clockwise and $n$ domains twisted counterclockwise. The number of all realizations belonging to the set $HEX^{mn}$ is $(m + n)!/m!n!$, where $m + n = 8$, and the corresponding total chirality charge is given by $q_{ch} = n - m$. If all chiral combinations are equiprobable, the value of the chirality charge should obey the well known binomial distribution

$$P(q_{ch} = n - m) = 2^{-n} \frac{(m + n)!}{m!n!}. \quad (8)$$

Taking into account all possible rotations and reflections, there are potentially several dozen different chiral states of 8 domains in the computational cell.

We define the empirical frequency of the event $q_{ch} = n - m$ as the number $s$ of successes (realizations of this event) divided by the total number of the performed SCFT runs, $k$. It is clear that the value of $s$ is the random variable, which is binomially distributed with parameters $p = P(q_{ch} = n - m)$ (probability of success) and $k$ (number of runs). Thus, the empirical frequency ν, its mean E[ν] and variance $\sigma^2$ are defined as

$$\nu = s/k, \quad E[\nu] = p, \quad \sigma^2 = p(1 - p)/k. \quad (9)$$

Table 1 shows the theoretical values of the probability distribution of the chirality charge and the predicted empirical frequencies with their standard deviations found in our series of SCFT runs with independent starts.

Except for the extreme values of the chirality charge (+8 and −8), the deviation of the empirical frequencies from the binomial distribution is of the order of the standard error. The deviations outside the 3σ confidence interval observed for the extreme values of the chirality charge may result from a weak interaction between neighboring columnar domains. Thus, the

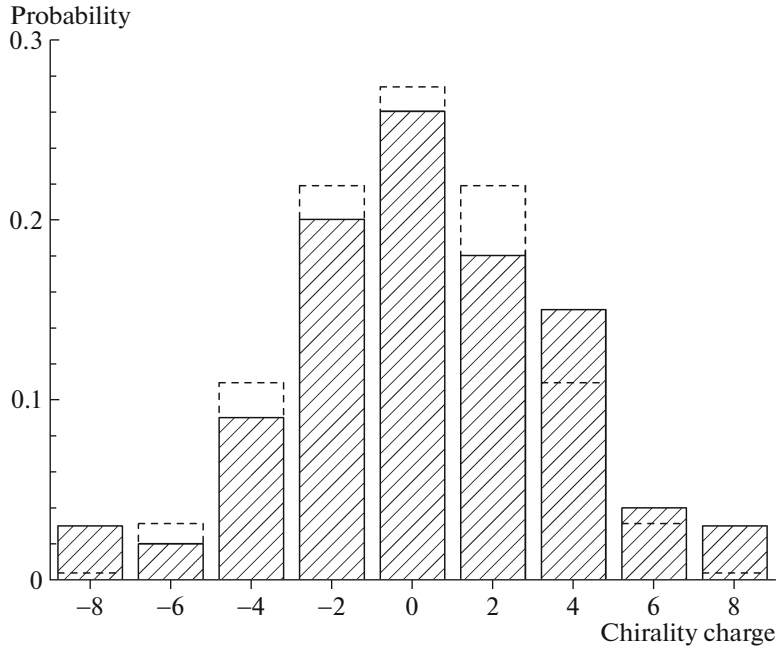


**Fig. 6.** Distribution of the chirality charge $q_{ch}$: theoretical probability (dashed line), empirical frequency (solid line).

hypothesis that the system forms a racemic mixture of chiral cylinders, seems plausible. The chirality charge distribution is shown in Fig. 6.

The solid line denotes the empiric distribution found in our SCFT calculations, and the dashed line corresponds to the theoretical binomial distribution. It seems evident that with an increase in the number of cylinders in the cell, the distribution of the chirality charge will become increasingly narrow, tending to the delta function centered at the origin.

In our previous work [22, 27, 28], we hypothesized that the chiral hexagonal mesophase is 3D macroscopically homochiral and that chirality arises from an achiral state as a result of spontaneous symmetry breaking with random selection of the twist direction. However, as the present SCFT calculations reveal, the chirality of the hexagonal phase does not extend the whole periodic simulation cell in the lateral (XY) direction, thereby not showing a macroscopic three-dimensional character. An effective confinement of the rod-rich cylindrical domains surrounded by the coil-rich polymer matrix induces a locally chiral structure with random choice of the chirality charge for each of the domains. All structures belonging to this structural class have the same free energy within the calculation accuracy and, consequently, they are degenerate. Thus, the macroscopic system can exist in two enantiomeric forms, although necessarily as a racemic mixture with equal weights of right-handed and left-handed states in the absence of any external influences that might lead to a preference of one rather than the other. On the other hand, an individual cylindrical domain can in principle be arbitrarily long, so that in formal sense we can regard it as a macroscopically homochiral quasi-one-dimensional object.

### *Pseudo-Dynamical Evolution of Chirality*

It is accepted that the free energy obtained from SCFT calculations provides an accurate description even out of equilibrium, i.e., not close to a saddle point for a given set of parameters [7]. Based on this assumption, it is interesting to understand how chirality arises from the initial achiral state and how it evolves far from equilibrium. The density field, from which chirality is evaluated, is natural for building models of pseudo-dynamical (kinetic) evolution. We stress that the "SCFT dynamics" are not physical dynamics and that our goal here is simply to trace how local chirality changes in the course of the SCFT iterative process. Specifically, we will study in this subsection how the achiral hexagonal structure is transformed into a three-dimensional chiral morphology of twisted domains through spontaneous symmetry breaking. How the chiral bias propagates and transfers from molecular level to chiral superstructure or phase from self-assembly is very important for many chemical and biological processes.

The Picard iterative scheme can be interpreted as a kind of pseudo-dynamical nonequilibrium evolution, in which the local measure of chirality LCI varies depending on the number of iterations $t$. As an initial configuration, we took the hexagonal structure consisting of 8 achiral cylinders discussed in the previous subsection. The chirality index LCI was calculated separately for each of the 8 cylinders. For each itera-

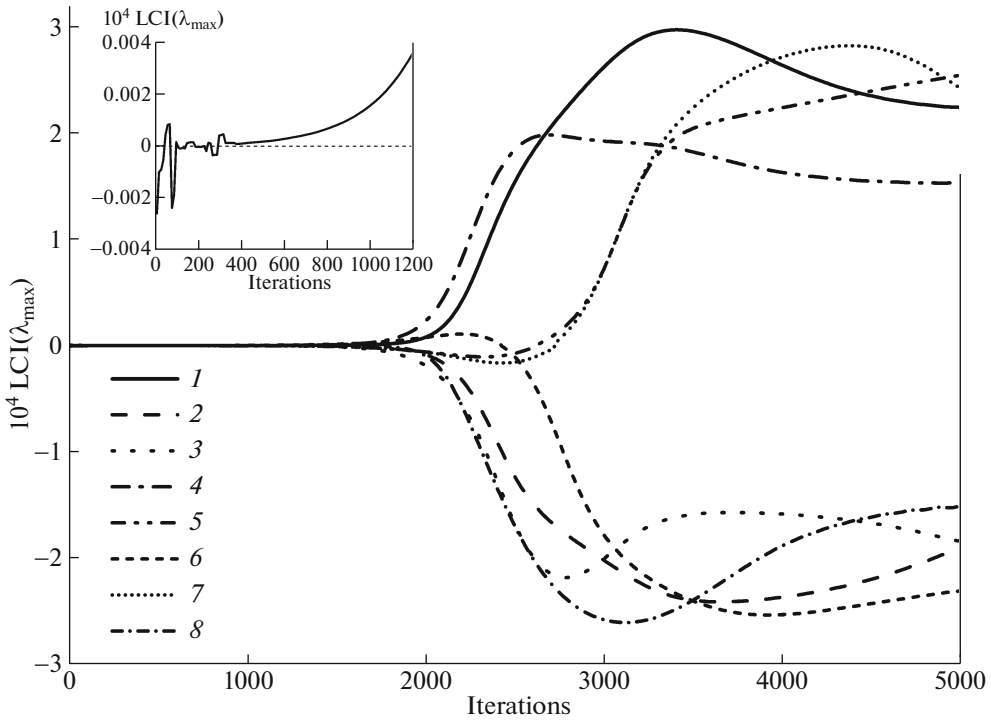


**Fig. 7.** Maximum absolute value of LCI (with its sign) as a function of the Picard iteration step for 8 columnar domains in the computation cell, at $f_C = 0.5$, $\chi N = 13.5$ and $\mu/\chi = 1.3$. Each curve refers to a single domain. The insert shows the evolution of chirality for one of the domains.

tion step, we determined the value of the linear scale $\lambda_{max}$ at which the absolute value of the LCI is maximal. The signed values of LCI($\lambda_{max}$) obtained in this way are shown in Fig. 7.

It is seen that within the first ≈1000 iterations, LCI($\lambda_{max}$) is close to zero. Then, the LCI($\lambda_{max}$) functions more and more deviate from zero and all the cylinders acquire clearly expressed twist direction: half of them is twisted clockwise, while the remaining half is twisted counterclockwise. Hence, the initial achiral state proved unstable for the used parameter set. The behavior of the system at the very early stages of evolution is of particular interest. The insert in Fig. 7 demonstrates the initial evolution of chirality for one of the domains. As seen, the system flips between the two chirality states at the initial stage of the evolutionary process: the LCI($\lambda_{max}$) value repeatedly changes its sign, passing through zero.

From the analysis of many pseudo-dynamic trajectories, we can conclude that the chirality sign is chosen randomly: each of the possible twist directions is equally likely to occur, but nevertheless only one of them is finally chosen. By selecting a particular direction in space, the orientational ordering of rigid blocks breaks the initial symmetry of the system. It seems, such a behavior is in line with the concept of spontaneous symmetry breaking (SSB), which is based on the assumption of the instability of the achiral state. The basic principles that guide such evolutionary scenario include the notion of statistical fluctuations, namely that in an initial achiral ensemble of a given type, there will always be an excess of one enantiomer, particularly apparent in small ensembles, and that such fortuitous excess may be greatly amplified. In other words, it is assumed that any arbitrarily small deviation of chirality from the instable achiral state can lead to a complete predominance of one of the chiral forms in the final state due to the mechanism of asymmetric ("autocatalytic-like") amplification building up upon initial imbalances in the right-handed and left-handed composition. This means that in the SSB scenario, the "sign of chiral purity" is the result of remembering a random choice of the sign of the small fluctuations with the subsequent amplification of this choice.

However, as our data indicate, not all small symmetry violations are amplified over a non-equilibrium evolution to reach the final chirally-pure state. It turns out that there is no ability to amplify all weak chiral fluctuations at the initial stage; instead, we more likely observe a bifurcation process in which there exists some waiting time $t^*$ for the onset of irreversible changes in chirality. Even if symmetry violations happen at $t < t^*$, in relation to the possibility of "evolutionary recovery", the situation in a certain sense is still "reversible". On the other hand, when $t > t^*$, any random choice of a given chiral sign, even with a very

small amplitude of the degree of chirality, becomes final and irreversible. The subsequent system evolution is controlled precisely by this small chirality amount, which is a necessary prerequisite for the irreversible violation of mirror symmetry. As can be expected, the reason for this amplification is that the achiral medium "follows" the locally induced helicity, which adjusts to itself the rigid polymer segments within a single rod-rich domain. In a sense, such cooperative behavior evokes associations with the well known "Sergeants-and-Soldiers" principle [47]: as a few sergeants can control the movements of large numbers of soldiers, so do the few ordered regions control the packing of large numbers of the remaining unordered rods, the latter unable to escape this influence.

Based on the data presented in subsections *Chirality in the strong segregation regime* and *Global and local chirality* (cf. also Fig. 5), we can speculate that the initiation of chirality may be attributed to the ordering of rods near the rod/coil interface. Chiral symmetry breaking in a system of achiral molecules at a liquid-solid interface is known for molecules with certain symmetry characteristics [48].

## CONCLUDING REMARKS

We have investigated at different length scales the properties of the chiral hexagonal nanostructures arising as a result of the interplay between orientational ordering and microphase separation in the system of diblock rod-coil copolymers (RCCs) with achiral blocks. Major results obtained in the present paper can be summarized as follows.

1. Based on the liquid-crystalline model of Semenov and Vasilenko [35], we have developed a simple theoretical approach that makes it possible to describe the structure formation in diblock copolymers containing strongly segregated flexible and rigid blocks. It was shown that in the strong segregation regime, nearly compositionally symmetric RCCs should form a columnar structure with twisted domains, whereas there is an interesting suppression of the lamellar morphologies with respect to the columnar one. This is due to a delicate balance between the interfacial free energy and the elastic stretching energy of the flexible coil blocks with a certain anisotropy of the elastic properties. Chirality in the columnar domains is induced by a twist in the relative orientation of the rods, which propagates over macroscopic distances along the domain.

2. The high-resolution three-dimensional SCFT simulations, coupled with calculations of the degree of chirality were used to quantify a range of chiral properties of the hexagonal mesophase with twisted domains. The interactions and the excluded volume effects were treated in an approximate manner via the Flory–Huggins repulsive interaction between the blocks, the Maier–Saupe mean field orientational interaction accounting for a thermotropic isotropic-nematic transition and the incompressibility constraint. It was demonstrated that chirality in the unit cell of the hexagonally packed cylinder phase can develop in two different ways, leading to the formation of either homochiral state or heterochiral (locally chiral) state. Thus, chiral polarization, which occurs when the rigid and flexible blocks are strongly incompatible, causes a transition to two degenerate chiral states.

3. Our large cell SCFT calculations performed for the system containing 8 columnar domains revealed that the chirality of the hexagonal phase does not extend the whole periodic simulation cell in the lateral direction, thereby not showing a macroscopic three-dimensional character. The magnitude of the cell chirality charge obeys the binomial distribution with random selection of the chirality charge (twist direction) for each of the rod-rich domains. We expect, therefore, that in a sufficiently large system, chiral cylinders should form a racemic mixture with equal weights of right-handed and left-handed states and the delta-function-like chirality charge distribution centered at zero. Although 3D homochirality is only the chance aided by luck, an individual domain can in principle be arbitrarily long, so that in formal sense we can regard it as a macroscopically homochiral quasi-one-dimensional object: a tendency to the confinement-induced twist at the molecular scale of rigid chain segments reshapes the structure and symmetry of the ordered state on much larger length scales.

4. We have discussed a model of pseudo-dynamical structural evolution aimed at understanding of how chirality arises from the initial achiral state and how it evolves far from equilibrium. In contrast to the standard scenario of spontaneous symmetry breaking, which assumes that the "sign of chiral purity" is the result of remembering a random selection of the sign of the small fluctuations occurring in the initial state with the subsequent amplification of this selection, our data indicate that not all small symmetry violations are amplified over a nonequilibrium evolution to reach the final chirality state. Instead, at the initial stage of the evolutionary process, there exists some waiting time for the onset of irreversible changes in chirality; during this time the system flips between the two chirality states.

## ACKNOWLEDGMENTS

The financial support from RFBR (project no. 16-03-00223) and the EU's 7th Framework Programme within the ERA.Net RUS Plus initiative (project nos. 01DJ15032 and 01DJ16020) is appreciated. IIP acknowledges the financial support from RFBR (project no. 16-29-05259) and the Government of the Russian Federation within Act 211, contract no. 02.A03.21.0011. The research was carried out using

the equipment of the shared research facilities of HPC computing resources at Moscow State University.

## REFERENCES


1. Q. Wang, Soft Matter **7**, 3711 (2011).
2. D. de las Heras, S. Varga, and F. J. Vesely, J. Chem. Phys. **134**, 214902 (2011).
3. S.-H. Lin, C.-C. Ho, and W.-F. Su, Soft Matter **8**, 4890 (2012).
4. H. Wu, L. He, X. Wang, and Y. Wang, Z. Jiang, Soft Matter **10**, 6278 (2014).
5. J.-H. Huang, Zh.-X. Fan, and Z.-X. Ma, J. Chem. Phys. **139**, 064905 (2013).
6. G. H. Fredrickson, V. Ganesan, and F. Drolet, Macromolecules **35**, 16 (2002).
7. G. H. Fredrickson, *The Equilibrium Theory of Inhomogeneous Polymers (International Series of Monographs on Physics)* (Oxford Univ. Press, New York, 2006).
8. R. R. Netz and M. Schick, Phys. Rev. Lett. **77**, 302 (1996).
9. M. W. Matsen and C. Barrett, J. Chem. Phys. **109**, 4108 (1998).
10. W. Li and D. Gersappe, Macromolecules **34**, 6783 (2001).
11. D. Duchs and D. E. Sullivan, J. Phys.: Condens. Matter **14**, 12189 (2002).
12. V. Pryamitsyn and V. Ganesan, J. Chem. Phys. **120**, 5824 (2004).
13. M. Shah, V. Pryamitsyn, and V. Ganesan, Macromolecules **41**, 218 (2008).
14. W. Song, P. Tang, H. Zhang, Y. Yang, and A.-C. Shi, Macromolecules **42**, 6300 (2009).
15. G. Yang, P. Tang, Y. Yang, and Q. Wang, J. Phys. Chem. B **114**, 14897 (2010).
16. W. Song, P. Tang, F. Qiu, Y. Yang, and A.-C. Shi, Soft Matter **7**, 929 (2011).
17. J. Gao, W. Song, P. Tang, and Y. Yang, Soft Matter **7**, 5208 (2011).
18. W. Song, P. Tang, F. Qiu, Y. Yang, and A.-C. Shi, J. Phys. Chem. B **115**, 8390 (2011).
19. X. Zhu, L. Wang, and J. Lin, J. Phys. Chem. B **117**, 5748 (2013).
20. J. Gao, P. Tang, and Y. Yang, Soft Matter **9**, 69 (2013).
21. S. Li, Y. Jiang, and J. Z. Y. Chen, Soft Matter **10**, 8932 (2014).
22. Yu. A. Kriksin and P. G. Khalatur, Macromol. Theory Simul. **21**, 382 (2012).
23. J. Tang, Y. Jiang, X. Zhang, D. Yan, and J. Z. Y. Chen. Macromolecules **48**, 9060 (2015).
24. X. Xu and Y. Jiang, Int. J. Mod. Phys. B **32**, 1840006 (2018).
25. J. Yu, F. Liu, P. Tang, F. Qiu, H. Zhang, and Y. Yang, Polymers **8**, 184 (2016).
26. Yu. A. Kriksin, S.-H. Tung, P. G. Khalatur, and A. R. Khokhlov, Polym. Sci., Ser. C **55**, 74 (2013).
27. P. G. Khalatur and A. R. Khokhlov, Soft Matter **9**, 10943 (2013).
28. Yu. A. Kriksin, P. G. Khalatur, and A. R. Khokhlov, "Supercomputer Simulation of Nanostructures in Copolymers with Flexible and Rigid Blocks," in *Supercomputing Technologies in Science, Education and Industry,* Ed. by V. A. Sadovnichiy, G. I. Savin, and V. V. Voevodin (Moscow Univ. Press, Moscow, 2014), pp. 145-154.
29. Yu. A. Kriksin, I. Ya. Erukhimovich, P. G. Khalatur, Yu. G. Smirnova, and G. ten Brinke, J. Chem. Phys. **128**, 244903 (2008).
30. Yu. A. Kriksin, P. G. Khalatur, I. Ya. Erukhimovich, G. ten Brinke, and A. R. Khokhlov, Soft Matter **5**, 2896 (2009).
31. Yu. A. Kriksin, P. G. Khalatur, I. V. Neratova, A. R. Khokhlov, and L. A. Tsarkova, J. Phys. Chem. C **115**, 25185 (2011).
32. V. I. Lebedev and D. N. Laikov, Dokl. Math. **59**, 477 (1999).
33. N. Sary, C. Brochon, G. Hadziioannou, and R. Mezzeng, Eur. Phys. J. E: Soft Matter Biol. Phys. **24**, 379 (2007).
34. L. Leibler, Macromolecules **13**, 1602 (1980).
35. A. N. Semenov and S. V. Vasilenko, Sov. Phys. JETP **63**, 70 (1986).
36. E. Helfand and Z. R. Wasserman, in *Developments in Block Copolymers,* Ed. by I. Goodman (Appl. Sci., New York, 1982), Vol. 1.
37. A. N. Semenov, Mol. Cryst. Liq. Cryst. **209**, 191 (1991).
38. W. Maier and A. Saupe, Z. Naturforsch., A: Astrtophys., Phys. Phys. Chem. **13**, 564 (1958).
39. B. Y. Drovetsky, A. J. Liu, and C. H. Mak, J. Chem. Phys. **111**, 4334 (1999).
40. M. A. Osipov, B. T. Pickup, and D. A. Dunmur, Mol. Phys. **84**, 1193 (1995).
41. M. Solymosi, R. J. Low, M. Grayson, and M. P. Neal, J. Chem. Phys. **116**, 9875 (2002).
42. M. P. Neal, M. Solymosi, M. R. Wilson, and D. J. Earl, J. Chem. Phys. **119**, 3567 (2003).
43. A. Pietropaolo, L. Muccioli, R. Berardi, and C. Zannoni, Proteins **70**, 667 (2008).
44. N. Weinberg and K. Mislow, Can. J. Chem. **78**, 41 (2000).
45. G. Millar, N. Weinberg, and K. Mislow, Mol. Phys. **103**, 2769 (2005).
46. S. Becke, S. Haller, M. A. Osipov, and F. Giesselmann, Mol. Phys. **108**, 573 (2010).
47. A. R. A. Palmans, J. A. J. M. Vekemans, E. E. Havinga, and E. W. Meijer, Angew. Chem., Int. Ed. Engl. **36**, 2648 (1997).
48. P. B. Kohl and D. L. Patrick, J. Phys. Chem. B **105**, 8203 (2001).